









Magnetic-field-induced robust zero Hall plateau state in MnBi_2Te_4 Chern insulator

Chang Liu ^{1,2,10}, Yongchao Wang ^{3,10}, Ming Yang ^{4,10}, Jiahao Mao¹, Hao Li^{5,6}, Yaoxin Li ¹, Jiaheng Li¹, Haipeng Zhu⁴, Junfeng Wang⁴, Liang Li⁴, Yang Wu ^{6,7}, Yong Xu ^{1,8,9✉}, Jinsong Zhang ^{1,9✉} & Yayu Wang ^{1,9✉}

The intrinsic antiferromagnetic topological insulator MnBi_2Te_4 provides an ideal platform for exploring exotic topological quantum phenomena. Recently, the Chern insulator and axion insulator phases have been realized in few-layer MnBi_2Te_4 devices at low magnetic field regime. However, the fate of MnBi_2Te_4 in high magnetic field has never been explored in experiment. In this work, we report transport studies of exfoliated MnBi_2Te_4 flakes in pulsed magnetic fields up to 61.5 T. In the high-field limit, the Chern insulator phase with Chern number $C = -1$ evolves into a robust zero Hall resistance plateau state. Nonlocal transport measurements and theoretical calculations demonstrate that the charge transport in the zero Hall plateau state is conducted by two counter-propagating edge states that arise from the combined effects of Landau levels and large Zeeman effect in strong magnetic fields. Our result demonstrates the intricate interplay among intrinsic magnetic order, external magnetic field, and nontrivial band topology in MnBi_2Te_4 .

¹State Key Laboratory of Low Dimensional Quantum Physics, Department of Physics, Tsinghua University, Beijing, China. ²Beijing Academy of Quantum Information Sciences, Beijing, China. ³Beijing Innovation Center for Future Chips, Tsinghua University, Beijing, China. ⁴Wuhan National High Magnetic Field Center and School of Physics, Huazhong University of Science and Technology, Wuhan, China. ⁵School of Materials Science and Engineering, Tsinghua University, Beijing, China. ⁶Tsinghua-Foxconn Nanotechnology Research Center, Department of Physics, Tsinghua University, Beijing, China. ⁷Department of Mechanical Engineering, Tsinghua University, Beijing, China. ⁸RIKEN Center for Emergent Matter Science, Wako, Saitama, Japan. ⁹Frontier Science Center for Quantum Information, Beijing, China. ¹⁰These authors contributed equally: Chang Liu, Yongchao Wang, Ming Yang. ✉email: yongxu@tsinghua.edu.cn; jinsongzhang@tsinghua.edu.cn; yayuwang@tsinghua.edu.cn

A remarkable breakthrough in the field of topological quantum matter is the discovery of topological insulators (TIs) with nontrivial bulk band topology and metallic boundary states^{1–8}. For two-dimensional (2D) TI with time-reversal symmetry (TRS), the helical edge states give rise to the quantum spin Hall (QSH) effect^{3,5,9–11}. When TRS is broken in magnetic TI, the quantum anomalous Hall (QAH) effect with chiral edge state emerges^{6–8,12–14}. Because the QAH effect originates from the topological Chern band rather than Landau levels^{13,14}, it is now called the Chern insulator phase to distinguish it from conventional quantum Hall (QH) insulator^{2,15,16}. Previous efforts on the Chern insulator mainly focused on its realization in zero magnetic field^{6–8,12}. An intriguing question that has yet to be addressed experimentally is the fate of the Chern insulator in ultra-high magnetic fields^{17,18}. It is likely that the QAH plateau will not survive forever because extreme conditions may induce other topological phases, as exemplified by the fractional QH effect¹⁹. Recently, it was demonstrated that helical phases analogous to the QSH phase exist in charge-neutral graphene^{20,21} and non-symmorphic KHgSb crystal²² in strong magnetic fields, which are characterized by quantized longitudinal resistance (R_{xx}) and zero Hall resistance (R_{yx}) plateau in certain magnetic fields and gate voltage (V_g) ranges. Inspired by these discoveries, it is imperative to find out the fate of the Chern insulator phase in MnBi_2Te_4 in strong magnetic fields, as has been discussed theoretically for magnetic TIs^{23,24}.

The recently discovered MnBi_2Te_4 combines intrinsic magnetism and nontrivial topology in one material^{25–37}, providing an ideal platform for exploring the topological phenomenon in extreme physical conditions. Figure 1a displays the schematic magnetic and crystal structure of MnBi_2Te_4 , where the Mn^{2+} magnetic moments have ferromagnetic (FM) alignments within each septuple layer (SL) and antiferromagnetic (AFM) coupling

between neighboring SLs. In the 2D limit, it exhibits the QAH insulator³⁰ and axion insulator²⁹ phases for odd-number and even-number of SLs. When FM order is induced by magnetic fields, the parity-time (PT) symmetry is broken and the bulk of MnBi_2Te_4 becomes a Weyl semimetal^{26,34,38}. In thin MnBi_2Te_4 flakes, the bulk Weyl semimetal band develops 2D quantum well states due to the quantum confinement along the c -axis. The topologically nontrivial quantum well subbands lead to a robust Chern insulator state with a quantized Hall plateau that persists to relatively high temperatures for magnetic field $\mu_0 H > 8 \text{ T}$ ^{29–31}. A unique feature of the Chern insulator phase in MnBi_2Te_4 lies in the negative sign of the Chern number ($C = -1$) in positive magnetization, which is distinguishable from the $C = +1$ Chern insulator phase in Cr-doped or V-doped TIs^{6–8,12}. Figure 1b illustrates the spatial configurations of the chiral edge state and the band structures for the two cases. Phenomenologically, the opposite sign of the Chern number arises from the opposite effective magnetic field due to the interplay between magnetic order and spin-orbit coupling^{39,40}. Because magnetic field couples with both magnetic moment and electron spin, for certain spin configurations of band structure, the combination of Landau levels and a sufficiently strong Zeeman energy may lead to topological quantum phenomena such as TRS-broken QSH effect or the quantum pseudospin Hall effect^{23,24} which have been proposed theoretically but never been realized in the experiment.

In this work, we report transport studies on exfoliated MnBi_2Te_4 in pulsed magnetic fields up to 61.5 T. Unexpectedly, the $C = -1$ phase evolves into a zero Hall plateau state characterized by a broad $R_{yx} = 0$ plateau and insulating R_{xx} in an ultrahigh magnetic field. Nonlocal transport measurements and theoretical calculations demonstrate the transport of this zero Hall plateau state is composed of two counter-propagating edge states with opposite Chern numbers, which arise from the FM

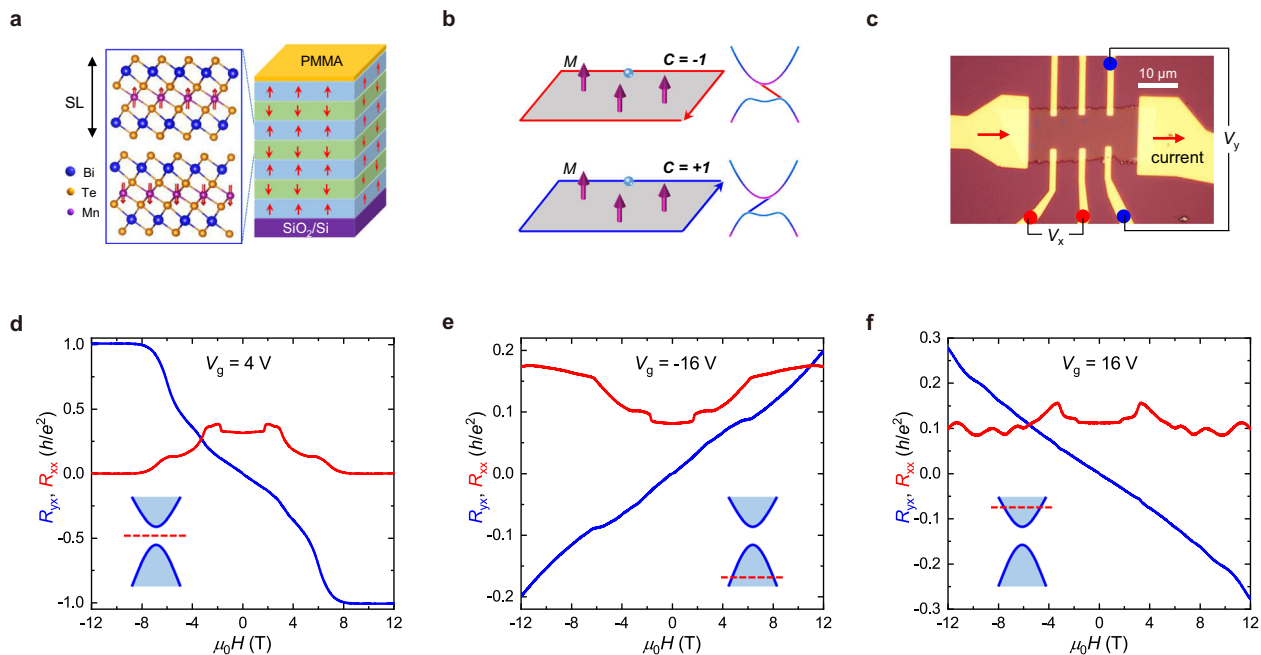


Fig. 1 Basic properties of a 7-SL MnBi_2Te_4 . **a** Schematic crystal and magnetic structures of the 7-SL MnBi_2Te_4 device. **b** Configurations of chiral edge state in the Chern insulator with Chern number $C = -1$ and $+1$. The opposite chirality of the edge state is marked by red and blue lines with arrows. The magenta arrows denote the magnetic moments. The schematic electronic structures for the two cases are shown on the right, with the opposite slope of the linear band representing opposite chirality. **c** Optical image of Device #7-SL-1 and the measurement setup. **d** Magnetic field dependent R_{xx} (red) and R_{yx} (blue) at $V_g = 4 \text{ V}$ and $T = 2 \text{ K}$. The Chern insulator phase is realized when the magnetic field is above 8 T, which is characterized by the $R_{yx} = -h/e^2$ plateau and $R_{xx} = 0$. **e** As V_g is tuned to -16 V , the transport is dominated by hole-type carriers. The jumps in R_{xx} at a magnetic field of around 1.8 T, 4 T, and 7 T correspond to the successive flips of Mn^{2+} moments in different SLs. **f** At $V_g = 16 \text{ V}$, the E_F is tuned to the conduction band and the transport exhibits characteristic features of the 2D electron gas. The insets in **d** to **f** roughly show the position of E_F at according to V_g .

order and the joint roles of Landau levels and Zeeman effect. The robust zero Hall plateau state represents a topological phenomenon that is unavailable in 2D electron-gas or hole-gas with conventional QH effect.

Results

The MnBi₂Te₄ devices studied in this work are mechanically exfoliated few-layer flakes fabricated into field-effect transistor devices on SiO₂/Si substrates that act as the bottom gate. The details of fabrication and transport measurements in pulsed magnetic fields are described in the method session. All the data in the main text are collected on a 7-SL device (#7-SL-1), and its photo is displayed in Fig. 1c. We first characterize the low-field transport properties at temperature $T = 2$ K in varied V_g , and three representative curves are shown in Fig. 1d to 1f (see Supplementary Fig. 1 for the full data set). The insets schematically illustrate the Fermi level (E_F) position for each V_g . The most pronounced feature is that for $V_g = 4$ V when E_F is in the Chern bandgap at FM state. At the low magnetic field side, R_{xx} exhibits three jumps due to the successive flips of Mn²⁺ moments, which is consistent with previous reports on few-layer MnBi₂Te₄ devices^{29–31}. Meanwhile, $|R_{yx}|$ progressively grows with the magnetic field, and the slope is mainly determined by the magnetization. A well-defined quantum plateau forms at $-h/e^2$ in R_{yx} for $\mu_0 H > 8$ T, accompanied by the rapid decrease of R_{xx} to zero. These are consistent with the Chern insulator behaviors in previously reports^{29–31}. As V_g is tuned away from 4 V to either side, E_F moves out of the bandgap, and carriers from the 2D subbands appear. The quantization of the Chern insulator phase is suppressed, and the negative (positive) slopes of the Hall traces at $V_g = +16$ V (-16 V) indicate the existence of electron (hole) type carriers. According to the linear slope, the mobility in the electron-type and the hole-type regime is estimated to be 3114 and 2098 cm²/Vs, respectively.

When we extend the transport measurements to much higher magnetic fields, some totally unexpected features start to emerge. According to the characteristic behavior of R_{yx} , the entire V_g range can be divided into four different regimes. As shown in Fig. 2a, the most remarkable feature of the high-field data is that the

$C = -1$ state only survives in a range of about 10 T. With further increase of magnetic fields, R_{yx} drops rapidly from the $-h/e^2$ plateau and, even more surprisingly, a very broad $R_{yx} = 0$ plateau forms in the high-field regime. Meanwhile, R_{xx} takes off from the zero value, develops a shoulder $\sim 0.5 h/e^2$ at the onset field of the zero plateau, and then increases again in higher magnetic fields. Remarkably, all the R_{xx} curves for varied V_g s tend to converge to the $0.5 h/e^2$ value (marked by the broken line) near the onset magnetic field of the zero Hall plateau. With the decrease of V_g , the high field zero Hall plateau is universally present and becomes even broader. As shown in Fig. 2b for V_g from -2 V and 0 V, the zero Hall plateau spans an incredibly wide field range from 10 T to the highest available field of 61.5 T. In Supplementary Fig. 2, we display the magnetic field-dependent R_{xx} and R_{yx} at $V_g = 4$ V for varied temperatures, in which a clear tendency of R_{xx} saturation at $0.5 h/e^2$ is observed at low temperatures. Both the $C = -1$ phase and the zero Hall plateau exhibit high robustness against thermal activation, even up to $T = 20$ K. Similar transport behaviors are also observed in other samples with different sizes and thicknesses (#7-SL-2 and #6-SL-1), as shown the Supplementary Fig. 3 to Fig. 7.

When V_g is decreased to more negative values, as shown in Fig. 2c, the Hall traces evolve to that characteristic of a 2D hole gas with an overall positive profile and growing amplitude from $V_g = -4$ V to -16 V. Meanwhile, R_{xx} reduces systematically as more holes are injected into the MnBi₂Te₄ flake. At $V_g = -16$ V, R_{yx} forms a well-defined Hall plateau at h/e^2 ($C = +1$) for $\mu_0 H > 40$ T, whereas R_{xx} drops to zero within experimental uncertainty. When V_g is tuned to the opposite side with V_g from 8 V to 16 V (Fig. 2d), quantized R_{yx} plateaus with Chern numbers $C = -3, -2,$ and -1 show up, along with apparent quantum oscillations. Remarkably, a unique feature here is that all the plateaus exhibit a strong tendency towards the zero Hall plateau state in the highest magnetic field, regardless of the position of E_F , which is quite unusual in conventional QH effect¹⁶.

Based on the high field data shown above, in Fig. 3a, b we depict the contour maps of R_{yx} and R_{xx} in the $\mu_0 H$ and V_g plane. The most prominent feature is that the zero Hall plateau state occupies the largest portion of the phase diagram. The magenta line marks the boundary between the $C = -1$ and zero Hall plateau state. The biggest puzzles revealed by the high field

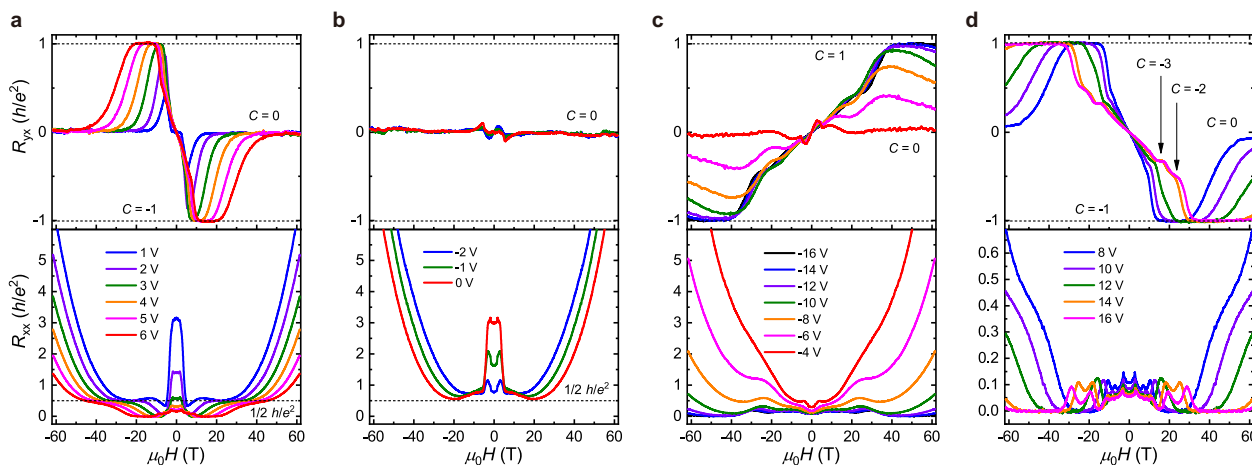


Fig. 2 Transport properties in pulsed magnetic field up to 61.5 T. **a** Magnetic field dependent R_{xx} and R_{yx} at $1 \text{ V} \leq V_g \leq 6 \text{ V}$. At $V_g = 4$ V, the $C = -1$ state is completely suppressed for $\mu_0 H > 30$ T, followed by the $C = 0$ state characterized by a broad zero Hall plateau. The black dashed line denotes the $R_{xx} = 0.5 h/e^2$ plateau. **b** Transport properties at $-2 \text{ V} \leq V_g \leq 0 \text{ V}$. Zero Hall plateau exist in a broad magnetic field range over 50 T. **c** Transport behaviors in the 2D hole gas regime. With the decrease of V_g , QH plateaus with a positive Chern number start to form. At $V_g = -16$ V, R_{yx} forms a wide Hall plateau at h/e^2 and R_{xx} drops to zero. **d** Characteristic transport behaviors of the 2D electron gas. With the increase of V_g from 8 V to 16 V, the $C = -1$ Hall plateau onsets at a higher magnetic field, becomes broader and approaches the $C = 0$ plateau only at the high-field limit. Electron-type QH plateaus with higher Chern numbers $C = -2$ and -3 also start to form.

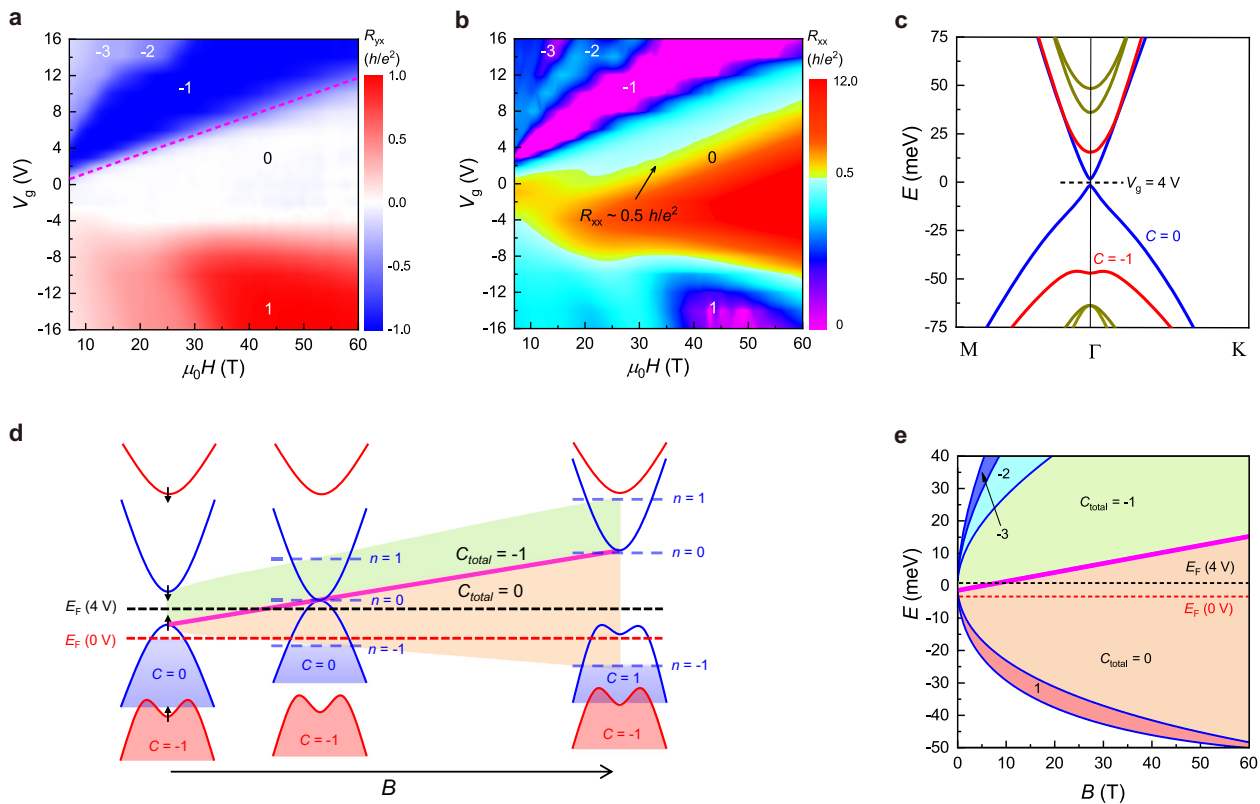


Fig. 3 Contour plots of experimental data and theoretical analysis of the $C = -1$ to $C = 0$ phase transition. **a, b** Experimental phase diagrams of R_{yx} and R_{xx} in the magnetic field and V_g plane. The $C = 0$ phase is the most stable ground state in a strong magnetic field. The magenta broken line denotes the boundary between the $C = -1$ and $C = 0$ phase. The black arrow represents the regime of $R_{xx} \sim 0.5 h/e^2$ for the helical Chern insulator phase. **c** Calculated band structure of 7-SL MnBi_2Te_4 along the M- Γ -K direction when the system is driven into the FM state. The red and blue lines denote the ferromagnetic-order induced Chern band ($C = -1$) and topologically trivial band ($C = 0$), respectively. **d** Schematic illustrations of the edge state formation and the band structure evolution in a magnetic field with Zeeman-effect-induced band inversion. The black and red dashed lines roughly mark the E_F position for $V_g = 4$ V and 2 V. The $C = -1$ to $C = 0$ phase transition occurs once band inversion happens. **e** Calculated Landau level spectrums with Zeeman-effect.

experiments are the nature of the zero Hall plateau state that prevails in the phase diagram and the underlying mechanism for the phase transition. In recent years, the zero Hall plateau states discovered in graphene and TI have attracted intense attentions^{22,41–43} for their nontrivial origins. However, most previous works focused on Hall conductivity (σ_{xy}) rather than Hall resistivity (ρ_{yx}). Because $\sigma_{xy} = \rho_{yx}/(\rho_{xx}^2 + \rho_{yx}^2)$, any kind of insulating state with large longitudinal resistivity ρ_{xx} can give rise to a $\sigma_{xy} = 0$ plateau. In contrast, the observation of $R_{yx} = 0$ plateau is very rare in experiments. Moreover, a zero Hall plateau state evolved from a Chern insulator or QH state is highly unusual.

The zero Hall plateau and the tendency of R_{xx} towards $0.5 h/e^2$ at the onset regime are highly reminiscent of the QSH effect, where the transport is conducted by a pair of helical edge states³. Differently, the helical transport in the QSH insulator is protected by TRS^{3,9,10}, i.e., the absence of both magnetic field and magnetic order. But here, the zero Hall plateau state is observed when both FM order in a strong magnetic field is present. Therefore, the zero Hall plateau state here represents a distinct insulator state that may host counter-propagating edge states transport with tunable scatterings in magnetic fields. To clarify this issue, we first calculate the band structure of 7-SL MnBi_2Te_4 when it is the FM state, as shown in Fig. 3c. According to theories, the breaking of PT-symmetry by FM order drives the bulk of MnBi_2Te_4 from an AFM TI into a Weyl semimetal^{26,34,38}. In the thin film case, the low-energy physics near E_F is described by four quantum well states, in analogy to the four-band model for the QAH effect in

magnetic TIs¹³. In these bands, one pair of subbands (red curves) is already inverted due to FM order, which is responsible for the $C = -1$ phase. The blue bands represent two trivial quantum-well states with an energy gap as small as 3 meV.

The most intuitive explanation for the magnetic-field-induced zero Hall plateau state is to consider the coexistence of a hole-type Landau level ($C = +1$) and the FM-order induced Chern band ($C = -1$). However, because Landau level spacing due to cyclotron motion increases in the magnetic field, the $C = -1$ phase for E_F lying in the bandgap will persist in a strong magnetic field. Apparently, this is inconsistent with the experimental observation of the $C = -1$ to zero Hall plateau transition. Therefore, it is indispensable to consider the band shift under the Zeeman effect. Because a small Zeeman energy insufficient for bandgap closing will not change the $C = -1$ phase in a certain V_g range with E_F located in the bandgap, a sufficiently large Zeeman effect that can cause a band inversion must be included to explain the absence of persistent $C = -1$ regime and the emergent zero Hall plateau state. The detailed illustrations of the band structure evolutions are displayed in Supplementary Fig. 8.

A closer examination of the spin configuration of each band reveals an enticing possibility of the Zeeman-effect induced band inversion, as shown in Fig. 3d. Because of the strong spin-orbit coupling in MnBi_2Te_4 , the z component of spin angular momentum s_z is no longer a good quantum number. Therefore, we label each state at the Γ point by the total angular momentum J_z , which is quantized by C_3 rotational symmetry and is mainly contributed by s_z because of the small orbital angular momentum

of p_z orbitals. The black arrows in the band structure denote the z component of J_z for each band at the Γ point. An important point is that spin-up refers to positive J_z or equivalently negative spin magnetic moment M_z . Thus, in an external magnetic field, along with the formation of Landau levels, bands with opposite J_z shift towards the opposite directions. When E_F initially lies near the top of the valence band (e.g., $V_g = 0$ V), the formation of $n = 0$ Landau level gives rise to a $C = +1$ chiral edge state. In combination with the original FM-order induced $C = -1$ band, a zero Hall plateau forms. Meanwhile, the Zeeman effect pushes the $n = 0$ Landau level upwards in a magnetic field, which leads to the $C = -1$ to zero Hall plateau transition for E_F lying the bandgap (e.g., $V_g = 4$ V). As the magnetic field is increased further, the Zeeman energy can surpass the gap size of the trivial bands, and a band inversion happens at some critical field. Meanwhile, at the gap closing point, the $n = 0$ Landau level crosses from the valence band to the inverted conduction band. Therefore, the total Chern number of the zero plateau state before and after band inversion does not change. The different shadows in Fig. 3d denote the regimes with different Chern numbers. This scenario is further supported by the calculated Landau level spectrums with the Zeeman effect taken into consideration, as highlighted by the upward phase boundary (magenta line) in Fig. 3e. In Supplementary Fig. 10, we also calculate the Landau level spectrum without the Zeeman effect, which displays apparently a qualitative departure from our experimental phase diagram.

For a better comparison with the previously discovered helical QH phase in graphene^{20,21}, we zoom in the R_{xx} and R_{yx} data in the Chern insulator regime, as displayed in Fig. 4a. At $V_g = 2$ V, the width of the $R_{xx} \sim 0.5 h/e^2$ plateau is as broad as 10 T. As V_g is increased to 4 V, the plateau becomes a broad shoulder. In the inset of Fig. 4a, we display the schematic illustrations of measurement setups and the evolution of counter-propagating edge states in a magnetic field. The opposite chirality of the two edge channels at the onset of the zero Hall plateau can naturally explain the zero Hall plateau and the quantized behaviors in R_{xx} . When the new $C = +1$ edge state just appears, its spatial distribution is not confined to the sample boundary⁴⁴. The scattering between the two counter-propagating edge states is weak, thus the R_{xx} value at the initial stage of the zero Hall plateau state is close to $0.5 h/e^2$ for scattering-immune helical transport, which is exactly the scenario for stabilizing the QSH edge state with broken TRS⁴⁴. With the further increase of the magnetic field, the edge states are pushed towards the boundaries. Because there is no TRS, the enhanced overlap between the two edge states leads to strong scatterings, giving rise to a rapid increase of R_{xx} . Similar situations of the deviations of R_{xx} in the high magnetic field are also observed in the helical QH phase in graphene^{20,21}.

To further validate the counter-propagating edge state nature of the zero Hall plateau state, we perform multiterminal and nonlocal transport measurements at $V_g = 4$ V, as displayed in Fig. 4b. The schematic setups of the measurements are shown in the insets. In the situation without scatterings between two edge states, the Landauer-Buttiker formalism renders $R_{2T} = 2 h/e^2$ and $R_{3T} = 1/2 h/e^2$. Because each pair of neighboring electrodes contributes a quantum resistance, the final resistance can be calculated by an effective circuit determined by the arrangement of electrodes between source and drain^{3,4}. The measured results exactly match such expectations, as marked by the magenta dashed lines. The middle and bottom panels show the results of two different setups for nonlocal measurements, which can directly detect edge state transport⁴. The measured $1/8 h/e^2$, $3/4 h/e^2$, and $1/4 h/e^2$ are the expected values for counter-propagating edge transport with weak scattering. At a high magnetic field where scatterings are enhanced, the zero Hall plateau state evolves towards a trivial insulator when the counter-propagating edge

states are fully canceled. However, the nonlocal transport data shows that even up to 61.5 T, there is still a sizeable edge state conduction. For the setup in the middle panel of Fig. 4b, at the onset of the zero Hall plateau when the scattering is weak, the ratio between local and nonlocal resistance is 1:4, which is fully determined by the electrode configurations. The ratio remains at 1:4 at a high magnetic field, which is a characteristic signature of edge state transport. Because a true trivial insulator has no edge conductivity, and residual carriers cannot give rise to such robust zero Hall plateau and do not contribute to any nonlocal signal, the zero Hall plateau state-observed here is a distinct insulator phase from a true trivial insulator. Reproducible non-local data with a much broader plateau width can be seen in another 7-SL sample (#7-SL-3) shown in Supplementary Fig. 11.

Discussion

The physical picture of emergent Chern band gaps induced by Landau levels and the Zeeman effect gives a comprehensive understanding of the zero Hall plateau state-observed here in thin flakes of MnBi_2Te_4 in strong magnetic fields. The key factor is to create a Chern bandgap in the magnetic field so that a new $C = +1$ edge state can be involved in transport. The Landau levels guarantee the formation of Chern band gaps inside the conduction or valence bands, whereas the Zeeman effect ensures the inversion of the original trivial bands in a magnetic field. Only in this case the universal tendency towards a zero Hall plateau state throughout the Chern insulator and the QH regimes can be well explained.

Naively, a zero Hall resistance in magnetic fields can be also attributed to other origins such as the coexistence of electron-hole puddles in a magnetic field. But a careful analysis of the transport data can rule it out. First, the zero Hall resistance due to the exact cancellation between electron and hole puddles is an accidental state that cannot form a broad $R_{yx} = 0$ plateau in a wide range of magnetic fields and V_g . It cannot explain the convergence of R_{xx} towards the $0.5 h/e^2$ plateau in the initial stage of zero Hall plateau state either. In addition, a trivial insulator is not a likely explanation either because it will exhibit diverging R_{yx} in the strong magnetic field in dc-transport measurement, rather than a broad zero Hall plateau^{45,46}. The presence of edge transport throughout the magnetic field regime, as well as the low-temperature saturation of R_{xx} for the different magnetic fields, also distinguish the zero Hall plateau state from a trivial insulator, as shown in Supplementary Fig. 2b. Notably, it is plausible that a spin-polarized edge mode with ballistic transport length beyond our longest channel length $\sim 10.8 \mu\text{m}$ emerges in a high magnetic field. It may also lead to a plateau-like feature with quantized R_{xx} . Further studies are required to completely rule out this possibility.

In conclusion, we realize a zero Hall plateau state in the MnBi_2Te_4 Chern insulator state when a strong magnetic field is applied. The robust zero Hall plateau against magnetic field and V_g , as well as the nonlocal transport measurements, suggest this state is composed of two counter-propagating edge states that arise from the emergence of a new Chern bandgap. The zero Hall plateau state discovered in the magnetic field in MnBi_2Te_4 represents a unique quantum transport phenomenon generated by the intricate interplay among intrinsic magnetism, external magnetic field, and nontrivial band topology.

Methods

Crystal growth. High-quality MnBi_2Te_4 single crystals were grown by a direct mixture of Bi_2Te_3 and MnTe with the ratio of 1:1 in a vacuum-sealed silica ampoule. After first heated to 973 K, the mixture is slowly cooled down to 864 K, followed by a long period of the annealing process. The phase and crystal quality are examined by X-ray diffraction on a PANalytical Empyrean diffractometer with $\text{Cu K}\alpha$ radiation.

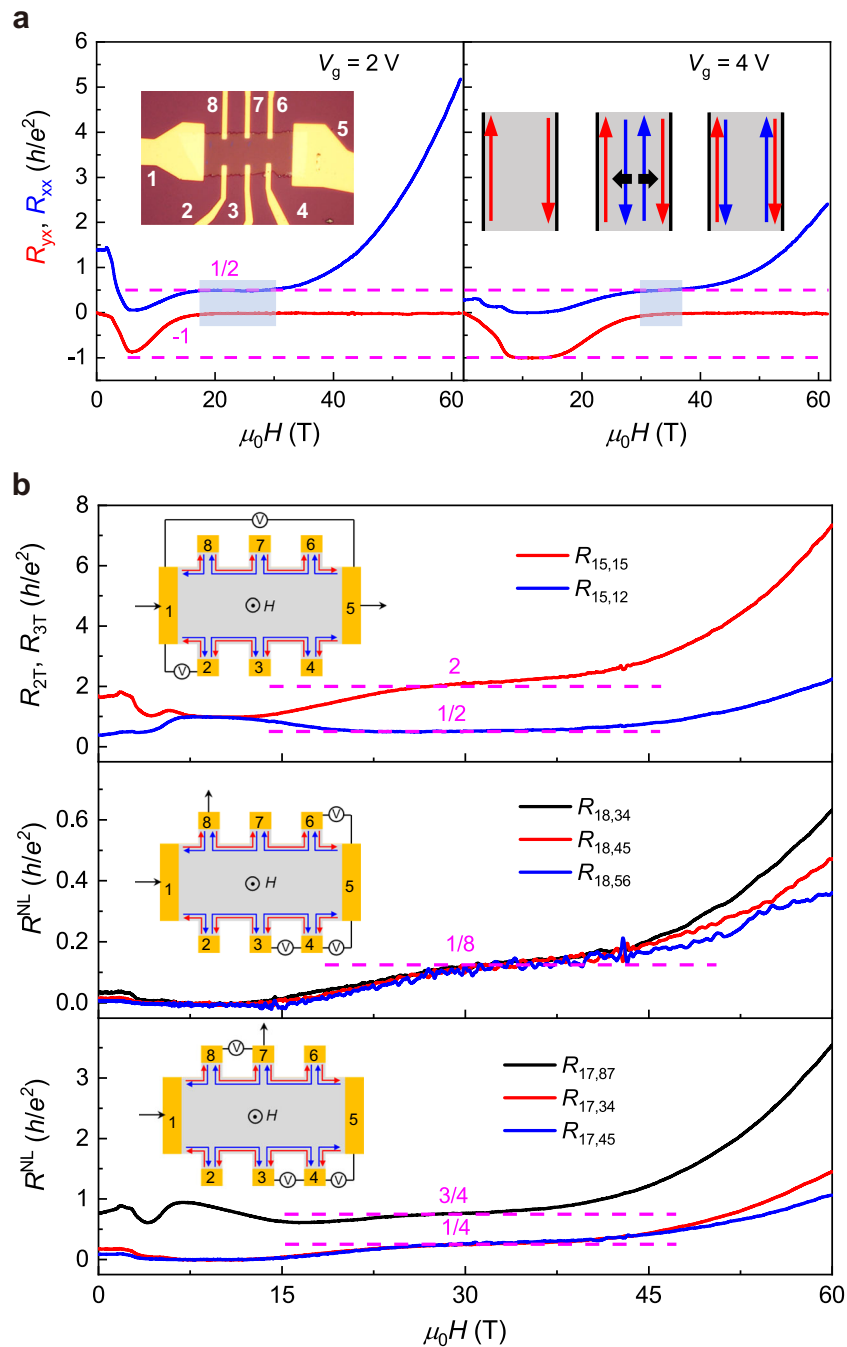


Fig. 4 Signatures of helical edge states transport in multiterminal and nonlocal measurements in the $C = 0$ phase. **a** Magnetic field dependent R_{xx} and R_{yx} near the $C = -1$ to $C = 0$ phase transition for $V_g = 2$ V and 4 V. The spatial distribution of edge states in the magnetic field is displayed in the inset. **b** Two-terminal, three-terminal, and nonlocal measurements in various configurations. The inset shows the schematic layout of the experimental setup. The expected values for R_{2T} and R_{3T} are $2 h/e^2$ and $1/2 h/e^2$, as denoted by the broken lines in the top panels. Middle panel: nonlocal measurements with current flowing through electrodes 1 and 8. The convergence of all three curves near $1/8 h/e^2$ (denoted by the broken lines) indicates the helical edge transport at the onset of the $C = 0$ phase. Bottom panel: nonlocal measurements in another setup with current flowing through electrodes 1 and 7. Depending on the position of the voltage probes, the resistance values of $1/4$ and $3/4 h/e^2$ are expected, which are confirmed by the experimental results.

Device fabrication. $MnBi_2Te_4$ flakes were mechanically exfoliated onto 285 nm-thick SiO_2/Si substrates by using the Scotch tape method. Before exfoliation, all SiO_2/Si substrates were pre-cleaned in air plasma for 5 min with ~ 125 Pa pressure. Thick flakes around the target sample area were manually scratched off by using a sharp needle. A 270 nm thick Poly(methyl methacrylate) (PMMA) layer was spin-coated on the exfoliated film before electron-beam lithography (EBL). After the EBL, 53 nm thick metal electrodes (Cr/Au, 3/50 nm) were deposited using a thermal evaporator connected to an argon-filled glove box with the O_2 and H_2O levels lower than 0.1 PPM. Throughout the fabrication and sample transfer process, the device was covered by PMMA to avoid direct contact with air. Four devices

with 7-SL and 6-SL $MnBi_2Te_4$ denoted as device #7-SL-1, #7-SL-2, #7-SL-3 and #6-SL-1 were measured in a pulsed magnetic field. The data shown in the main figures are taken from device #7-SL-1, and that of other devices are documented in Supplementary Fig. 1 to Fig. 11.

Transport measurement. High-field electrical transport measurements were performed in a 4He cryostat with a base temperature of 2 K in Wuhan National High Magnetic Field Center. A pulsed DC current of $4 \mu A$ was generated by a Yokogawa GS610 current source. An uncertainty of 250Ω arising from the high

rate of field sweep (1000 T/s) in pulsed magnetic field measurements and imperfect cancellation of measurement circuit was estimated according to the real geometry of the circuit. The absence of hysteresis in low-field transport data of the 7-SL MnBi₂Te₄ samples is due to the fast field sweeping rate. Low-field calibration of the 6-SL thick device was performed in a commercial ⁴He cryostat with a superconducting magnet up to 9 T. The longitudinal and Hall voltages were measured simultaneously by using lock-in amplifiers with an AC current of 200 nA generated by a Keithley 6221 current source. The back gate was applied by a Keithley 2400 source meter. To eliminate the effect of electrode misalignment, the measured four-terminal longitudinal and transverse resistances were symmetrized and anti-symmetrized with respect to the magnetic field.

Theoretical calculation. First-principles calculations were performed in the framework of density functional theory (DFT) using the Vienna ab initio Simulation Package⁴⁷. The plane-wave basis with an energy cutoff of 350 eV was adopted, in combination with the projected augmented wave (PAW) method. The Monkhorst-Pack *k*-point mesh of 9 × 9 × 3 was adopted in the self-consistent calculation with the inclusion of spin-orbit coupling. The modified Becke-Johnson (mBJ) functional⁴⁸ was employed to improve the description of the electronic band structure in the ferromagnetic (FM) MnBi₂Te₄ bulk. The DFT-D3 method⁴⁹ was used to describe van der Waals (vdW) interactions between neighboring septuple layers in MnBi₂Te₄. The tight-binding models derived from the FM bulk were used to model thin films. Maximally localized Wannier functions were constructed from first-principles calculations of the FM bulk, and the tight-binding Hamiltonian of the FM bulk was obtained. Then, tight-binding Hamiltonians of thin films were constructed by cutting slabs from the bulk. Band structures, topological properties, edge state calculations⁵⁰, and effective *k*-*p* Hamiltonians of MnBi₂Te₄ thin films were computed based on the tight-binding Hamiltonians.

Data availability

All raw and derived data used to support the findings of this work are available from the authors on request.

Received: 9 May 2021; Accepted: 12 July 2021;

Published online: 30 July 2021

References

- Moore, J. E. The birth of topological insulators. *Nature* **464**, 194–198 (2010).
- Haldane, F. D. M. Nobel lecture: topological quantum matter. *Rev. Mod. Phys.* **89**, 040502 (2017).
- König, M. et al. Quantum spin Hall insulator state in HgTe quantum wells. *Science* **318**, 766–770 (2007).
- Roth, A. et al. Nonlocal transport in the quantum spin Hall state. *Science* **325**, 294–297 (2009).
- Knez, I., Du, R. R. & Sullivan, G. Evidence for helical edge modes in inverted InAs/GaSb quantum wells. *Phys. Rev. Lett.* **107**, 136603 (2011).
- Chang, C. Z. et al. Experimental observation of the quantum anomalous Hall effect in a magnetic topological insulator. *Science* **340**, 167–170 (2013).
- Checkelsky, J. G. et al. Trajectory of the anomalous Hall effect towards the quantized state in a ferromagnetic topological insulator. *Nat. Phys.* **10**, 731–736 (2014).
- Kou, X. et al. Scale-invariant quantum anomalous Hall effect in magnetic topological insulators beyond the two-dimensional limit. *Phys. Rev. Lett.* **113**, 137201 (2014).
- Bernevig, B. A., Hughes, T. L. & Zhang, S. C. Quantum spin Hall effect and topological phase transition in HgTe quantum wells. *Science* **314**, 1757–1761 (2006).
- Kane, C. L. & Mele, E. J. Quantum spin Hall effect in graphene. *Phys. Rev. Lett.* **95**, 226801 (2005).
- Kane, C. L. & Mele, E. J. Z₂ topological order and the quantum spin Hall effect. *Phys. Rev. Lett.* **95**, 146802 (2005).
- Chang, C. Z. et al. High-precision realization of robust quantum anomalous Hall state in a hard ferromagnetic topological insulator. *Nat. Mater.* **14**, 473–477 (2015).
- Liu, C. X., Qi, X. L., Dai, X., Fang, Z. & Zhang, S. C. Quantum anomalous Hall effect in Hg_{1-y}Mn_yTe quantum wells. *Phys. Rev. Lett.* **101**, 146802 (2008).
- Yu, R. et al. Quantized anomalous Hall effect in magnetic topological insulators. *Science* **329**, 61–64 (2010).
- Haldane, F. D. M. Model for a quantum Hall-effect without Landau-levels-condensed-matter realization of the parity anomaly. *Phys. Rev. Lett.* **61**, 2015–2018 (1988).
- Vonklitzing, K. The quantized Hall-effect. *Rev. Mod. Phys.* **58**, 519–531 (1986).
- Böttcher, J., Tutschku, C. & Hankiewicz, E. M. Fate of quantum anomalous Hall effect in the presence of external magnetic fields and particle-hole asymmetry. *Phys. Rev. B* **101**, 195433 (2020).
- Böttcher, J., Tutschku, C., Molenkamp, L. W. & Hankiewicz, E. M. Survival of the quantum anomalous Hall effect in orbital magnetic fields as a consequence of the parity anomaly. *Phys. Rev. Lett.* **123**, 226602 (2019).
- Tsui, D. C., Stormer, H. L. & Gossard, A. C. Two-dimensional magnetotransport in the extreme quantum limit. *Phys. Rev. Lett.* **48**, 1559–1562 (1982).
- Young, A. F. et al. Tunable symmetry breaking and helical edge transport in a graphene quantum spin Hall state. *Nature* **505**, 528–532 (2014).
- Veyrat, L. et al. Helical quantum Hall phase in graphene on SrTiO₃. *Science* **367**, 781–786 (2020).
- Liang, S. et al. A gap-protected zero-Hall effect state in the quantum limit of the non-symmorphic metal KHgSb. *Nat. Mater.* **18**, 443–447 (2019).
- Yang, Y. et al. Time-reversal-symmetry-broken quantum spin Hall effect. *Phys. Rev. Lett.* **107**, 066602 (2011).
- Li, H. C., Sheng, L. & Xing, D. Y. Quantum phase transitions in ultrathin films of three-dimensional topological insulators in the presence of an electrostatic potential and a Zeeman field. *Phys. Rev. B* **85**, 045118 (2012).
- Gong, Y. et al. Experimental realization of an intrinsic magnetic topological insulator. *Chin. Phys. Lett.* **36**, 076801 (2019).
- Li, J. et al. Intrinsic magnetic topological insulators in van der Waals layered MnBi₂Te₄-family materials. *Sci. Adv.* **5**, eaaw5685 (2019).
- Otrokov, M. M. et al. Prediction and observation of an antiferromagnetic topological insulator. *Nature* **576**, 416–422 (2019).
- Rienks, E. D. L. et al. Large magnetic gap at the Dirac point in Bi₂Te₃/MnBi₂Te₄ heterostructures. *Nature* **576**, 423–428 (2019).
- Liu, C. et al. Robust axion insulator and Chern insulator phases in a two-dimensional antiferromagnetic topological insulator. *Nat. Mater.* **19**, 522–527 (2020).
- Deng, Y. et al. Quantum anomalous Hall effect in intrinsic magnetic topological insulator MnBi₂Te₄. *Science* **367**, 895–900 (2020).
- Ge, J. et al. High-Chern-number and high-temperature quantum Hall effect without Landau levels. *Natl. Sci. Rev.* <https://doi.org/10.1093/nsr/nwaa089>.
- Cui, J. H. et al. Transport properties of thin flakes of the antiferromagnetic topological insulator MnBi₂Te₄. *Phys. Rev. B* **99**, 155125 (2019).
- Otrokov, M. M. et al. Unique thickness-dependent properties of the van der Waals interlayer antiferromagnet MnBi₂Te₄ films. *Phys. Rev. Lett.* **122**, 107202 (2019).
- Zhang, D. et al. Topological axion states in the magnetic insulator MnBi₂Te₄ with the quantized magnetoelectric effect. *Phys. Rev. Lett.* **122**, 206401 (2019).
- Yan, J. Q. et al. Crystal growth and magnetic structure of MnBi₂Te₄. *Phys. Rev. Mater.* **3**, 064202 (2019).
- Lee, S. H. et al. Spin scattering and noncollinear spin structure-induced intrinsic anomalous Hall effect in antiferromagnetic topological insulator MnBi₂Te₄. *Phys. Rev. Res.* **1**, 012011 (2019).
- Zhang, S. et al. Experimental observation of the gate-controlled reversal of the anomalous Hall effect in the intrinsic magnetic topological insulator MnBi₂Te₄ device. *Nano Lett.* **20**, 709–714 (2020).
- Li, J. et al. Magnetically controllable topological quantum phase transitions in the antiferromagnetic topological insulator MnBi₂Te₄. *Phys. Rev. B* **100**, 121103 (2019).
- Morimoto, T., Furusaki, A. & Nagaosa, N. Topological magnetoelectric effects in thin films of topological insulators. *Phys. Rev. B* **92**, 085113 (2015).
- Nagaosa, N., Sinova, J., Onoda, S., MacDonald, A. H. & Ong, N. P. Anomalous Hall effect. *Rev. Mod. Phys.* **82**, 1539–1592 (2010).
- Checkelsky, J. G., Li, L. & Ong, N. P. Zero-energy state in graphene in a high magnetic field. *Phys. Rev. Lett.* **100**, 206801 (2008).
- Xu, Y. et al. Observation of topological surface state quantum Hall effect in an intrinsic three-dimensional topological insulator. *Nat. Phys.* **10**, 956–963 (2014).
- Yoshimi, R. et al. Quantum Hall states stabilized in semi-magnetic bilayers of topological insulators. *Nat. Commun.* **6**, 8530 (2015).
- Li, H. C. et al. Stabilization of the quantum spin Hall effect by designed removal of time-reversal symmetry of edge states. *Phys. Rev. Lett.* **110**, 266802 (2013).
- Kivelson, S., Lee, D. H. & Zhang, S. C. Global phase diagram in the quantum Hall effect. *Phys. Rev. B* **46**, 2223–2238 (1992).
- Hilke, M. et al. Experimental evidence for a two-dimensional quantized Hall insulator. *Nature* **395**, 675–677 (1998).
- Kresse, G. & Furthmüller, J. Efficient iterative schemes for ab initio total-energy calculations using a plane-wave basis set. *Phys. Rev. B* **54**, 11169 (1996).
- Becke, A. D. & Johnson, E. R. A simple effective potential for exchange. *J. Chem. Phys.* **124**, 221101 (2006).
- Grimme, S., Antony, J., Ehrlich, S. & Krieg, H. A consistent and accurate ab initio parametrization of density functional dispersion correction (DFT-D) for the 94 elements H–Pu. *J. Chem. Phys.* **132**, 154104 (2010).
- Wu, Q. S., Zhang, S. N., Song, H. F., Troyer, M. & Soluyanov, A. A. WannierTools: an open-source software package for novel topological materials. *Comput. Phys. Commun.* **224**, 405–416 (2018).

Acknowledgements

This work is supported by the Basic Science Center Project of NSFC (grant No. 51788104) and the National Key R&D Program of China (grants No. 2018YFA0307100 and No. 2018YFA0305603). This work is additionally supported by the NSFC (grants No. 12004122, No. 51991340 and No. 21975140). This work is supported in part by the Beijing Academy of Quantum Information Sciences (BAQIS) and the Beijing Advanced Innovation Center for Future Chip (ICFC).

Author contributions

Y.Y.W., J.S.Z., and Y.X. supervised the research. C.L., Y.C.W., and Y.X.L. fabricated the devices and performed the transport measurements. M.Y., H.P.Z., J.F.W., and L.L. were in charge of the pulsed magnet facility. H.L. and Y.W. grew the MnBi_2Te_4 crystals. J.H.M., J.H.L., and Y.X. performed first-principles calculations. C.L., J.S.Z., Y.X., and Y.Y.W. prepared the manuscript with comments from all authors.

Competing interests

The authors declare no competing interests

Additional information

Supplementary information The online version contains supplementary material available at <https://doi.org/10.1038/s41467-021-25002-x>.

Correspondence and requests for materials should be addressed to Y.X., J.Z. or Y.W.

Peer review information *Nature Communications* thanks the anonymous reviewers for their contribution to the peer review of this work. Peer reviewer reports are available.

Reprints and permission information is available at <http://www.nature.com/reprints>

Publisher's note Springer Nature remains neutral with regard to jurisdictional claims in published maps and institutional affiliations.



Open Access This article is licensed under a Creative Commons Attribution 4.0 International License, which permits use, sharing, adaptation, distribution and reproduction in any medium or format, as long as you give appropriate credit to the original author(s) and the source, provide a link to the Creative Commons license, and indicate if changes were made. The images or other third party material in this article are included in the article's Creative Commons license, unless indicated otherwise in a credit line to the material. If material is not included in the article's Creative Commons license and your intended use is not permitted by statutory regulation or exceeds the permitted use, you will need to obtain permission directly from the copyright holder. To view a copy of this license, visit <http://creativecommons.org/licenses/by/4.0/>.

© The Author(s) 2021